Increased Retinal Oxygen Metabolism Precedes Microvascular Alterations in Type 1 Diabetic Mice

Wenzhong Liu,[1] Shoujian Wang,[2] Brian Soetikno,[1] Ji Yi,[3] Kevin Zhang,[1] Siyu Chen,[1] Robert A. Linsenmeier,[1,4,5] Christine M. Sorenson,[6] Nader Sheibani,[2] and Hao F. Zhang[1,4]

[1]Department of Biomedical Engineering, Northwestern University, Evanston, Illinois, United States
[2]Departments of Ophthalmology and Visual Science, University of Wisconsin, Madison, Wisconsin, United States
[3]Department of Medicine, Boston University, Boston, Massachusetts, United States
[4]Department of Ophthalmology, Northwestern University, Chicago, Illinois, United States
[5]Department of Neurobiology, Northwestern University, Evanston, Illinois, United States
[6]Department of Pediatrics, University Wisconsin, Madison, Wisconsin, United States

Purpose. To investigate inner retinal oxygen metabolic rate (IRMRO$_2$) during early stages of type 1 diabetes in a transgenic mouse model.

Methods. In current study, we involved seven diabetic mice (Akita/+, TSP1$^{-/-}$) and seven control mice (TSP1$^{-/-}$), and applied visible-light optical coherence tomography (vis-OCT) to image functional parameters including retinal blood flow rate, oxygen saturation (sO$_2$) and the IRMRO$_2$ value longitudinally from 5 weeks of age to 13 weeks of age. After imaging at 13 weeks of age, we analyzed the imaging results, and examined histology of mouse retina.

Results. Between diabetic mice and the control group, we observed significant differences in venous sO$_2$ from 9 weeks of age ($P = 0.006$), and significant increment in IRMRO$_2$ from 11 weeks of age ($P = 0.001$) in diabetic mice compared with control group. We did not find significant differences in retinal blood flow rate as well as arterial sO$_2$ during imaging between diabetic and control mice. Histologic examination of diabetic and control mice at 13 weeks of age also revealed no anatomical retinal alternations.

Conclusions. In diabetic retinopathy, complications in retinal oxygen metabolism may occur before changes of retinal anatomical structure.

Keywords: oxygen saturation, retinal blood flow, optical coherence tomography, retinal metabolism

Diabetic retinopathy (DR) is one of the leading blindness-causing diseases. If left unchecked, DR will progress to permanent retinal vascular alterations, including hemorrhage and proliferative neovascularization.[1] Such alterations threaten vision and eventually lead to blindness.[2] Because a clinical tool does not exist that reliably detects DR in its very early stages, current clinical care targets DR in the late stages,[3] when vision problems are already present. Recovery from late-stage DR is, however, problematic. Furthermore, the health care costs have almost doubled for treating DR with microvascular complications.[4] It is thus necessary to better understand DR pathogenesis, which will enable early diagnosis, optimal medical intervention, and novel drug development.

Retinal oxygen metabolic rate (IRMRO$_2$) might be a key biomarker to investigate DR pathogenesis,[5] because complications of IRMRO$_2$ are present among different stages of DR and sensitive to development of DR. In early diabetes, oxidative stress in the retina can influence retinal cellular oxygen metabolism,[6] thus potentially triggering variations of IRMRO$_2$. In DR, retinal microvasculature abnormalities,[7] including capillary wall thickening[8] and vessel tortuosity,[9] may affect retinal perfusion and oxygen delivery, changing the IRMRO$_2$.[10] In addition, the retina is nourished by both the retinal and choroidal vascular systems. Both early diabetes and DR can influence the perfusion of choroidal circulation,[11] which may

further affect retinal oxygen metabolism. Therefore, quantification of IRMRO$_2$ is important to understand DR; however, IRMRO$_2$ studies are difficult. First, it is challenging to investigate IRMRO$_2$ on patients with early DR due to the difficulty in defining DR stages among diabetes patients. Second, DR is a dynamic disease; IRMRO$_2$ can change along the progress of DR. Thus, the imaging time point could influence the measured results of IRMRO$_2$. Third, IRMRO$_2$ requires measuring both retinal blood flow and oxygen saturation (sO$_2$) simultaneously and precisely.[12] The lack of an accurate, noninvasive detection modality will bias IRMRO$_2$ measurements. For instance, measuring retinal sO$_2$ is difficult with multi-wavelength fundus photography[13] because of the signal degradation due to light scattering. The recently developed multi-wavelength photoacoustic ophthalmoscope (PAOM) shows promise in generating an accurate retinal sO$_2$ reading[12]; however, physical contact between the acoustic transducer and the eyeball in PAOM will be inconvenient and limit its applications. The aforementioned challenges, including unclear definitions of DR stages, inconsistent imaging time points, and unreliable imaging tools, have prevented investigation of IRMRO$_2$ in DR.

No existing animal model can mimic all the features of DR in humans; however, several animal models have been developed to mimic some aspects of human DR, especially for the early
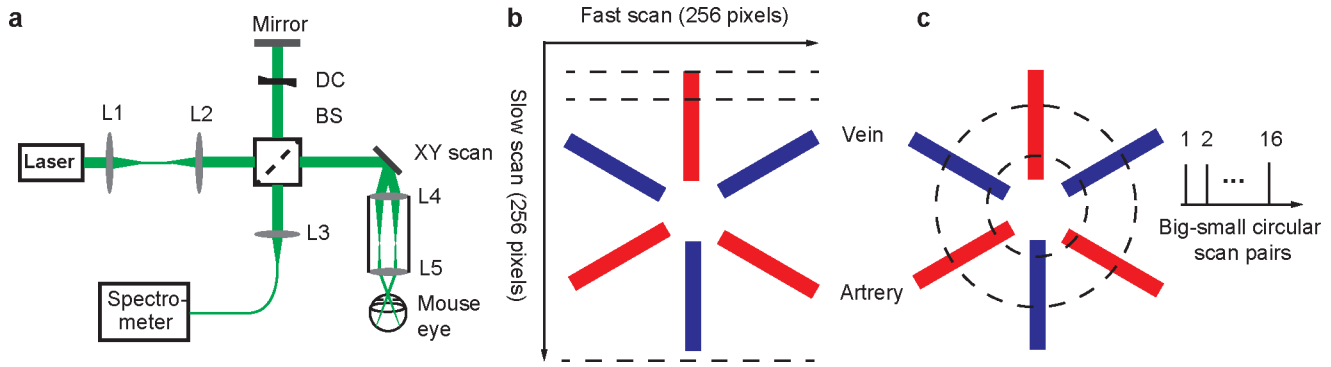
FIGURE 1. Experimental setup and scanning protocols. (**a**) The implemented vis-OCT. (**b**) Raster-scanning protocol to acquire the retinal fundus image and measure retinal oxygen saturation (sO_2). (**c**) Dual-ring scanning protocol to measure retinal blood flow. L1 to L5 are lenses; BS, beam splitter; DC, dispersion compensation.

stages of DR.[14,15] In this study, we used type-1 diabetic Akita/+ mice, which lacked thrombospondin-1 (TSP1) (Akita/+, TSP1^{−/−}) as our model of early-stage DR. Consistent with type 1 diabetes, the Akita/+ mouse is known to have hyperglycemia, hypoinsulinemia, polydipsia, and polyuria by 4 weeks of age.[16] The mice reach diabetic levels of hyperglycemia (>250 mg/dL) by week 8. In addition to their diabetes, the Akita/+ mice also develop features consistent with early-stage DR. Namely, by 7 months of age, they exhibit pericyte cell (PC) loss and acellular capillaries.[16] Beyond 6 months, retinal neovascularization, a feature of late-stage human DR, has been shown in the Akita/+ mouse.[17] The TSP1 deficiency, in addition to the Akita/+, exacerbates all of the features of early-stage DR (eg, PC loss, acellular capillaries) in the original Akita/+ model.

To investigate whether IRMRO$_2$ could serve as a biomarker for early DR, we longitudinally monitored the IRMRO$_2$ in the Akita/+, TSP1^{−/−} mouse using newly developed visible-light optical coherence tomography (vis-OCT).[18,19] We measured the retinal sO_2 and total blood flow rate in diabetic and control mice, every other week from 5 weeks to 13 weeks of age. Nondiabetic TSP1^{−/−} mice with normal retinal vasculature served as controls.[16] From the longitudinal blood flow and oxygen measurements, we established the IRMRO$_2$ in diabetic and control mice and drew comparisons. The present study demonstrates vis-OCT as a potentially useful imaging tool for measuring the IRMRO$_2$ in early DR.

METHODS

Visible-Light OCT System and Scanning Protocol

The vis-OCT system enables the quantification of both retinal sO_2 and retinal blood flow in vivo.[19] Using a supercontinuum laser as a light source (center wavelength: 568.5 nm; bandwidth: 107 nm; SuperK NKT photonics, Birkerød, Denmark), we built a free-space spectral-domain (SD)-OCT (Fig. 1a) with the theoretical axial resolution being 1.3 µm in air. To quantify retinal sO_2, we raster-scanned 256 × 256 A-lines onto the mouse retina to acquire a retinal fundus image, covering a 1.05 × 1.05 mm^2 area centered at the optic disc (Fig. 1b). By analyzing the reflected light spectrum from each retinal vessel, we determined the corresponding sO_2 value (Fig. 2). To quantify the retinal blood flow, we measured the phase shifts, vessel size, and Doppler angles (Fig. 3) using a dual-ring scanning protocol (Fig. 1c). In total, 16 pairs of small-big rings were scanned onto a mouse retina centered at the optic disc. The radius was 0.31 mm for the big scanning ring, and 0.21
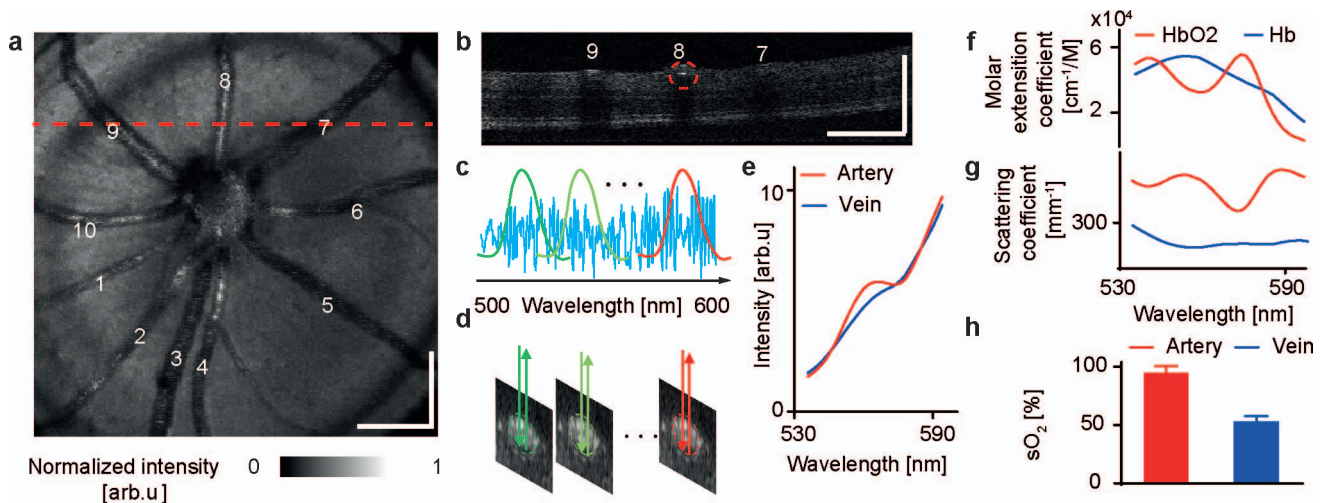

FIGURE 2. Quantification of retinal blood oxygen saturation. (**a**) Sample retinal fundus image with vessel index labeled. (**b**) Sample B-scan from the *red dashed line* in (**a**). (**c**) Short-time Fourier transforms with different center frequencies (*green, light green,* and *red*) performed on the spectral interferogram (*blue line*). (**d**) Sub-band B-scans of the vessel in (**b**) denoted by the *red dashed circle*. (**e**) Examples of the OCT signal spectrum from an artery and vein. (**f**) Molar extinction coefficient of oxygenated hemoglobin and deoxygenated hemoglobin specta. (**g**) Scattering coefficient of oxygenated hemoglobin and deoxygenated hemoglobin spectra. (**h**) Average sO_2 values for arteries and veins. *Scale bar*: 200 µm.
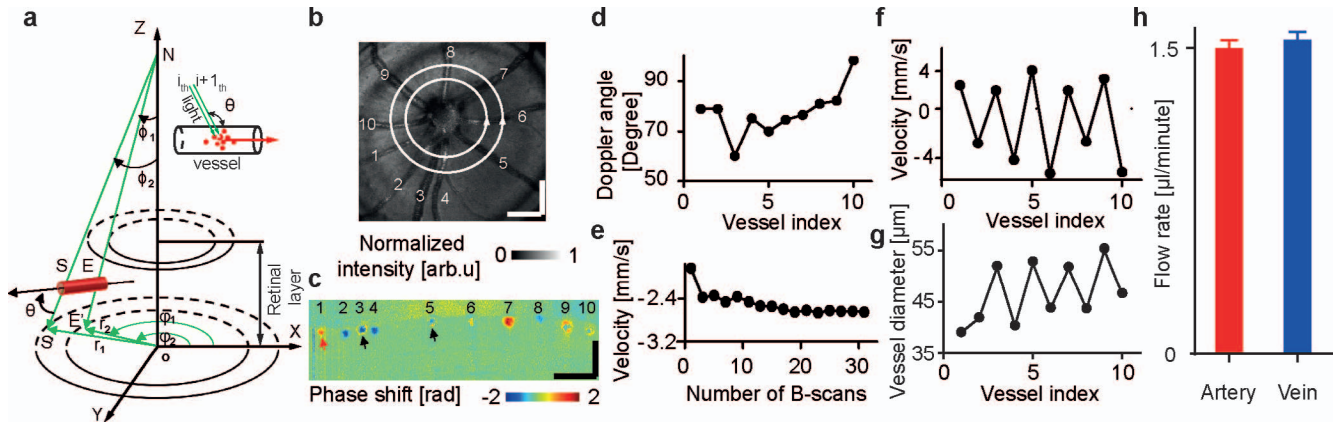
FIGURE 3. Illustration of blood flow quantification. (**a**) Schematic of dual-ring scanning. (**b**) Sample retinal fundus image with dual rings labeled. (**c**) Sample phase-shift B-scan image from the small scanning ring. (**d**) Calculated Doppler angles. (**e**) Stability of velocity after averaging across cumulative B-scans. (**f**) Mean velocities of 10 sample vessels for the retina. (**g**) Measured vessel diameters. (**h**) Total blood flow rate in the retinal arterial and venous vascular system. *Scale bar*: 200 μm.

mm for the small scanning ring, with 4096 A-lines in each ring. During the experiments, we first performed the raster-scanning, and then the dual-ring scanning protocol. The A-line rate was 25 kHz for both scanning protocols.

Quantification of Retinal sO₂

The procedure for retinal oximetry with vis-OCT was reported in great detail previously.[18] As shown in Figure 2, we raster-scanned the retina (Fig. 2a), and reconstructed the cross-sectional B-scan using the full band of the spectral interferogram. From the cross-sectional B-scan, we obtained the three-dimensional vessel coordinates (Fig. 2b). As illustrated in Figure 2c, short-time Fourier transforms (STFT), with different band center frequencies (depicted as the Gaussian-shaped colored curves), were performed on the spectral interferogram (blue line) to reconstruct sub-band B-scans. Examples of the obtained sub-band B-scans, for the circled vessel in Figure 2b, are shown in Figure 2d. The bandwidth for each of the STFTs was 15 nm, which reduced the axial resolution of each sub-band B-scan to 9.5 μm. Although the axial resolution was reduced, it is still sufficient to resolve the major murine retinal vessels, which have vessel diameters of 40 μm or more. Using the already determined vessel coordinates, we extracted the OCT signal from the bottom of the vessel across all the sub-band B-scans, as highlighted by the arrows in Figure 2d. Examples of the obtained OCT signal spectra, for an artery and a vein, are shown in Figure 2e.

To obtain the sO₂ from the OCT signal spectra, we needed to model the reflectance and attenuation of the OCT signal by using the optical attenuation coefficient of oxygenated hemoglobin (α_{HbO2}) and deoxygenated hemoglobin (α_{Hb}) as follows:

$$I^2 = I_0^2 R_0 r \exp\left(-2nd\alpha_{HbO2}(sO_2) - 2nd\alpha_{Hb}(1 - sO_2)\right). \quad (1)$$

Here I_0 is the incident intensity on the retina, and R_0 is the reflectance of the reference arm. The coefficient r denotes the reflectance from the blood vessel wall. The spectral behavior of r was as scattering under first-order Born approximation, which is given by the power law function: $r(\lambda) = A\lambda^{-\tau}$. Here, A and τ are constants. The exponential term in Equation 1 is attenuation according to Beer-Lambert's law, where n is the mean refractive index of the blood ($\sim$1.35), and α_{HbO2} and α_{Hb} denote the attenuation coefficients. The backscattered light experiences two-way (round-trip) attenuation through the

blood vessel diameter, d [μm], hence the factor of 2 in the exponential expression. The wavelength-dependent attenuation coefficients (α_{HbO2} and α_{Hb}) incorporate both the absorption coefficient (μ_a) and scattering coefficients (μ_s) of the whole blood (Figs. 2f, 2g). Considering the packing effects of red blood cells, our previous investigation[18] suggested the relationship between the attenuation coefficient, absorption coefficient, and scattering coefficient as follows:

$$\alpha_{HbO2} = \mu_{aHbO2} + 0.2\mu_{sHbO2}$$
$$\alpha_{Hb} = \mu_{aHb} + 0.2\mu_{sHb} \quad (2)$$

To obtain sO₂, the OCT signal spectra for each vessel was fit to a modified form of Equation 1 (see Appendix) using Least-Squares (LS) fitting. This retinal oximetry technique using vis-OCT has been validated in silico with Monte Carlo simulations,[20] in vitro with artificially oxygenated bovine blood and a commercial blood gas analyzer,[19] and in vivo with systemic hypoxia experiments and a commercial pulse oximeter.[19,21]

Quantification of Retinal Blood Flow Rate

The principles of retinal flow measurements using Doppler OCT have been reported previously.[12,20–23] Doppler SD-OCT can measure only the projected flow along the probing beam. To achieve the absolute flow measurements, the Doppler angle, which is the angle between the probing beam and blood flow, must be measured in addition to the projection Doppler shift.[12] We used the dual-ring scanning protocol to simultaneously extract the projected flow and Doppler angle.[12] Figure 3a shows the geometry of the dual-ring scanning protocol. Using this geometry, equations for the Doppler angle θ were derived (see Appendix). From the equations, we see that the Doppler angle requires the three-dimensional vessel axis coordinates, hence the requirement for two circular rings in the dual-ring method. Figure 3b shows an example of a mouse fundus with the scanning paths of the dual rings. Figure 3d shows the calculated Doppler angles of all the vessels in this example retina.

After acquiring the Doppler angles, we calculated the absolute retinal blood flow velocity v (m/s) as follows[12]:

$$v = \frac{f_{sample}\lambda_0\Delta\phi}{4\pi n\cos(\theta)}, \quad (3)$$

where f_{sample} (kHz) is the A-line rate; λ_0 (nm) is the center wavelength of the SD-OCT; $\Delta\phi$ is the phase shift (rad) (Fig. 3c)

between adjacent A-lines after bulk motion correction; n is the refractive index of the sample ($n = 1.35$); and θ [degree] is the Doppler angle. We observed phase-wrapping (Fig. 3c) in experiments; to correct this, the axial blood flow direction is necessary. The flow direction is recognizable from the phase shifts near the vessel border, where low flow velocity prevents phase-wrapping. Assuming the actual phase $\Delta\phi < 0$, we corrected the phase-wrapping as follows[24]:

$$\Delta\phi = \begin{cases} \Delta\phi, & \Delta\phi < 0 \\ \Delta\phi - 2\cdot\pi, & \Delta\phi > 0 \end{cases} \qquad (4)$$

For the actual phase that is $\Delta\phi > 0$, we corrected the phase-wrapping as

$$\Delta\phi = \begin{cases} \Delta\phi, & \Delta\phi > 0 \\ \Delta\phi + 2\cdot\pi, & \Delta\phi < 0 \end{cases} \qquad (5)$$

In this study, we had 16 pairs of big-small ring scanning, providing 32 continuous B-scans. We tested the measured velocity stability by averaging the velocity results across different cumulative B-scans and comparing the mean velocity difference between adjacent cumulative B-scans. We considered the velocity stable if the velocity difference was smaller than 0.1 mm/s between adjacent cumulative B-scans. After averaging results across 20 B-scans (Fig. 3e), stable velocity was achieved. The velocities for the sample retina are shown in Figure 3f, where the arterial flow has positive velocities running from the optic disc to the peripheral retina, and the venous flow has negative velocities draining blood from the peripheral retina to the optic disk.

We measured the vessel diameter *Dia* (m) in the axial direction in the OCT B-scan structural, the actual vessel diameter *Dia_r* (m) was:

$$Dia\_r = Dia \times \sin(\theta), \qquad (6)$$

where θ (radians) is the Doppler angle. The measured vessel diameters for the sample retina are given in Figure 3g. The vessel cross-sectional area Z (m^2) was:

$$Z = \pi \times \frac{Dia\_r^2}{4}. \qquad (7)$$

With the absolute velocity and vessel size, the corresponding blood flow in the i_{th} vessel was determined:

$$F_i = v_i \times A_i, \qquad (8)$$

where v_i is the average velocity and A_i is the vessel cross-sectional area.

We calculated the total blood flow (F [μL/min]) by summing all blood flow in the retinal arterial/vein vascular system, as shown in Equation 9:

$$F = \sum_{i=1}^{N} F_i, \qquad (9)$$

where N is the total number of retinal arteries or veins.

Calculation of IRMRO$_2$

The *IRMRO$_2$* (g/min) calculation was described in our previous article.[12] We calculated the *IRMRO$_2$* as follows:

$$IRMRO_2 = \frac{4 \times W_{O2}}{W_{HbO2}} \times [HbT] \times (sO_{2a} - sO_{2v}) \times F, \qquad (10)$$

where W_{O2} and W_{HbO2} are the molecular weights of O$_2$ and oxygenated hemoglobin, which were 32 and 68,000 (g/mol),

respectively. [HbT] is the hemoglobin concentration in the mouse, which was measured to be 150 (g/L); sO_{2a} and sO_{2v} are the mean sO_2 values in the artery and vein vascular system, respectively. F (μL/min) is the total retinal flow.

The unit of *IRMRO$_2$* in Equation 10 is ng/min. We can convert ng/min to L/min as:

$$V = n_g \times R \times T / P, \qquad (11)$$

where V is the volume of gas; n_g is the number of moles of gas; R is 8.3145 (J·mole^{-1}·K^{-1}); T is the blood temperature (311.15 K); and P is the standard atmospheric pressure (101,325 Pa). Statistic results were obtained from seven Akita/+, TSP1$^{-/-}$ DR mice and seven TSP1$^{-/-}$ control mice, respectively.

Retinal Vessel Preparation and Endothelial Cell (EC) Density and PC Density Quantification

Retinal vessel sample preparation and EC, PC quantification can be found in our previous article.[16] In this study, all retinal vessel preparations, EC and PC number counting were performed on 13-week-old mice. We fixed mouse eyes in 4% paraformaldehyde for 24 hours, bisected equatorially, and removed the entire retina. The retinas were washed overnight in distilled water and incubated in 3% trypsin (Trypsin 1:250; Difco, BD Diagnostic Systems, Sparks, MD, USA) prepared in 0.1 M Tris, 0.1 M maleic acid, 0.2 M NaF for approximately 1.0 to 1.5 hours at 37°C. There was 0.2 M sodium fluoride in the digestion buffer to inhibit DNases from contaminating the crude trypsin preparation. After digestion, the retinal vessels were flattened by four radial cuts and mounted on glass slides for Periodic Acid-Schiff and hematoxylin staining.

We used nuclear morphology to distinguish PCs from ECs. The nuclei of ECs are oval or elongated in shape, laid within the vessel wall, and extended along the axis of the capillary; in comparison, pericyte nuclei are typically small, spherical in shape, and stain densely. Generally, the pericyte nuclei is characterized by a protuberant position on the capillary wall.[16] We determined the number of ECs and PCs by counting nuclei under the microscope with ×400 magnification, where the mounting reticle (10 × 10 μm) was placed in one of the viewing oculars to facilitate counting. We included only retinal capillaries in the mid-zone for the cell count, and measured the number of ECs and PCs in four reticles from the four quadrants of each retina. The mean value of ECs and PCs for each retina was determined by averaging the values from the four reticles.

Assessment of Acellular Capillaries

The method can be found in our previous article.[16] Briefly, we counted acellular capillaries in five field areas in the middle of the retina samples (×200 magnification). Acellular capillaries were defined as capillary-sized vessel tubes without nuclei anywhere along their length. Tubes with a diameter <20% of the diameter of adjacent capillaries were identified as strands and were not counted.

Animal Anesthetic Procedure

We weighed each mouse before imaging, and anesthetized them by intraperitoneal injection with a cocktail of ketamine (87 mg/kg body weight) and xylazine (13 mg/kg body weight).[25] During the experiment, we applied 0.5% tetracaine hydrochloride ophthalmic solution to paralyze the iris sphincter muscle and 1% tropicamide ophthalmic solution to dilate the pupil. Commercial artificial tears (Systane; Alcon Laboratories, Inc., Fort Worth, TX, USA) were added every minute to the mouse cornea to prevent dehydration and cataract

formation. The blood sO_2 were measured to be approximately 98 and the heart rate was approximately 320 beats per minute (Pulse oximetry, Model 8500AV; Nonin Medical, Inc., Plymouth, MN, USA). All experimental procedures were in compliance with the ARVO Statement for the Use of Animals in Ophthalmic and Vision Research, and the laboratory animal protocol approved by the Institutional Animal Care and Use Committee at Northwestern University. Ocular safety with vis-OCT has been previously confirmed.[19,26]

Blood Glucose Measurements

Blood glucose levels were measured with a commercial available glucometer (Glucometer Elite; Bayer, Inc., Whippany, NJ, USA) by using a drop of tail blood collected from mice models.

RESULTS

Histologic Examination Finds No Microvascular Structural Complications in Early-Stage Diabetic Mice

We monitored the body weight and blood glucose levels for both diabetic and control nondiabetic mice from 5 weeks to 13 weeks of age, as shown in Figure 4. During the imaging window, the body weights were comparable between the diabetic and control groups. We also noted that at 13 weeks of age, the weights of the diabetic mice were slightly less than the control mice (25.1 ± 1.0 vs. 28.5 ± 2.0 g) (Fig. 4a). Higher blood glucose levels (Fig. 4b) were observed in the diabetic mice at 5 weeks of age compared with normal blood glucose levels in the control mice (205 ± 7 vs. 132 ± 6.5 mg/dL). After the final imaging at 13 weeks of age, we examined histology of the retinal microvasculature in both the diabetic and control mice. We found no retinal acellular capillaries or PC loss in the diabetic mice (Figs. 4c, 4d); both the diabetic and control mice had similar retinal EC density and PC density (Fig. 4e). These results suggested a healthy microvasculature in early-stage diabetic mice.

Longitudinal Imaging Reveals Increased Retinal Oxygen Metabolism in Early Diabetic Mice

We used vis-OCT to quantify the retinal sO_2,[18,21] blood flow rate,[20] and $IRMRO_2$[19] simultaneously (Fig. 1). To resolve the retinal sO_2, we first extracted the light reflectance spectrum from each vessel, and then fitted the extracted light reflectance spectrum with the known absorption/scattering spectra of both oxygenated and deoxygenated hemoglobin based on a modified Beer-Lambert law[18] (Fig. 2; Methods). The fitting gave an sO_2 reading for each vessel. To calculate retinal blood flow rate,[12] we first extracted flow-induced phase shifts, then calculated the Doppler angle for each retinal vessel and measured the corresponding vessel diameter. Finally, with these measurements, the absolute flow rate was quantified (see Fig. 3; Methods).

An outline of longitudinal imaging is provided in Figure 5a. Longitudinal retinal imaging for both the diabetic and control groups was performed every other week, from 5 to 13 weeks of age. At each imaging time point, we measured seven physiological parameters, including blood velocity, vessel diameter, blood flow rate, arterial sO_2, venous sO_2, artery-vein sO_2 difference, and $IRMRO_2$, as shown in Figures 5b through 5h. By comparing results between the diabetic group and control group, we tried to determine the changes in each measured parameter over time. First, we did not find
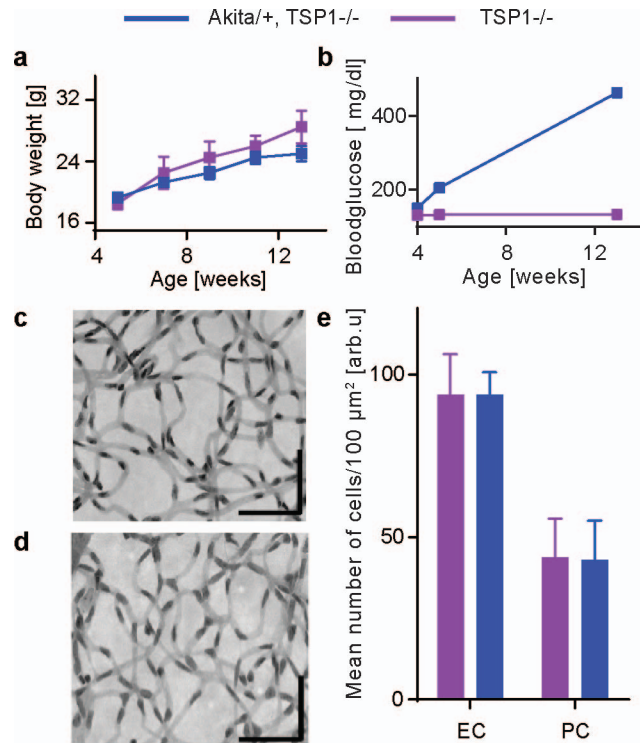

FIGURE 4. Comparison of body weights, blood glucose levels, and EC and PC densities between diabetic and control groups. (**a**) Body weight comparison between diabetic and control mice from 5 to 13 weeks of age. (**b**) Comparison of blood glucose between diabetic and control mice from 4 to 13 weeks of age. (**c**) Sample retinal vessels from diabetic mouse group at 13 weeks of age. (**d**) Sample retinal vessels from control mouse group at 13 weeks of age. (**e**) Comparison of PC and EC density between diabetic and control mice. *Scale bar*: 50 μm.

significant differences in blood velocity or arterial sO_2 between the diabetic mice and control mice ($P \geq 0.128$ for velocity, and ≥ 0.09 for arterial sO_2; see Supplementary Table S1) (Figs. 5b, 5d). These two parameters, blood velocity and arterial sO_2, were also stable (less than 4% variation) over the course of the experiment within both the diabetic mice and control mice. Second, we did not find significant differences in vessel diameter or blood flow rate between the diabetic mice and control mice ($P \geq 0.128$ for diameter, and ≥ 0.26 for flow rate; see Supplementary Table S1). However, we observed a moderate increase in vessel diameter (4 [μm] in absolute value or 10% in relative percentage increase) and blood flow rate (0.2 [μL/min] in absolute value or 13% in relative percentage increase) in the diabetic mice over the course of experiments. Such increases were not present in the control mice (less than 3% in relative percentage change) (Figs. 5c, 5f). Third, between the diabetic mice and control mice, we observed significant differences in venous sO_2 and artery-vein sO_2 difference from 9 weeks of age ($P = 0.006$; see Supplementary Table S1), and significant differences in $IRMRO_2$ from 11 weeks of age ($P = 0.001$; see Supplementary Table S1). Across the course of experiments in diabetic mice, we also found significant changes in the venous sO_2 (9.6 [%] in absolute decrease or 16% in relative percentage decrease), artery-vein sO_2 difference (9.0 [%] in absolute increase or 27.9% in relative percentage increase) and $IRMRO_2$ (54.45 [nL/min] in absolute increase or 41.3% in relative percentage increase). In comparison, during the course of experiments in the control mice, we found stable values among venous sO_2, artery-vein sO_2 difference, and
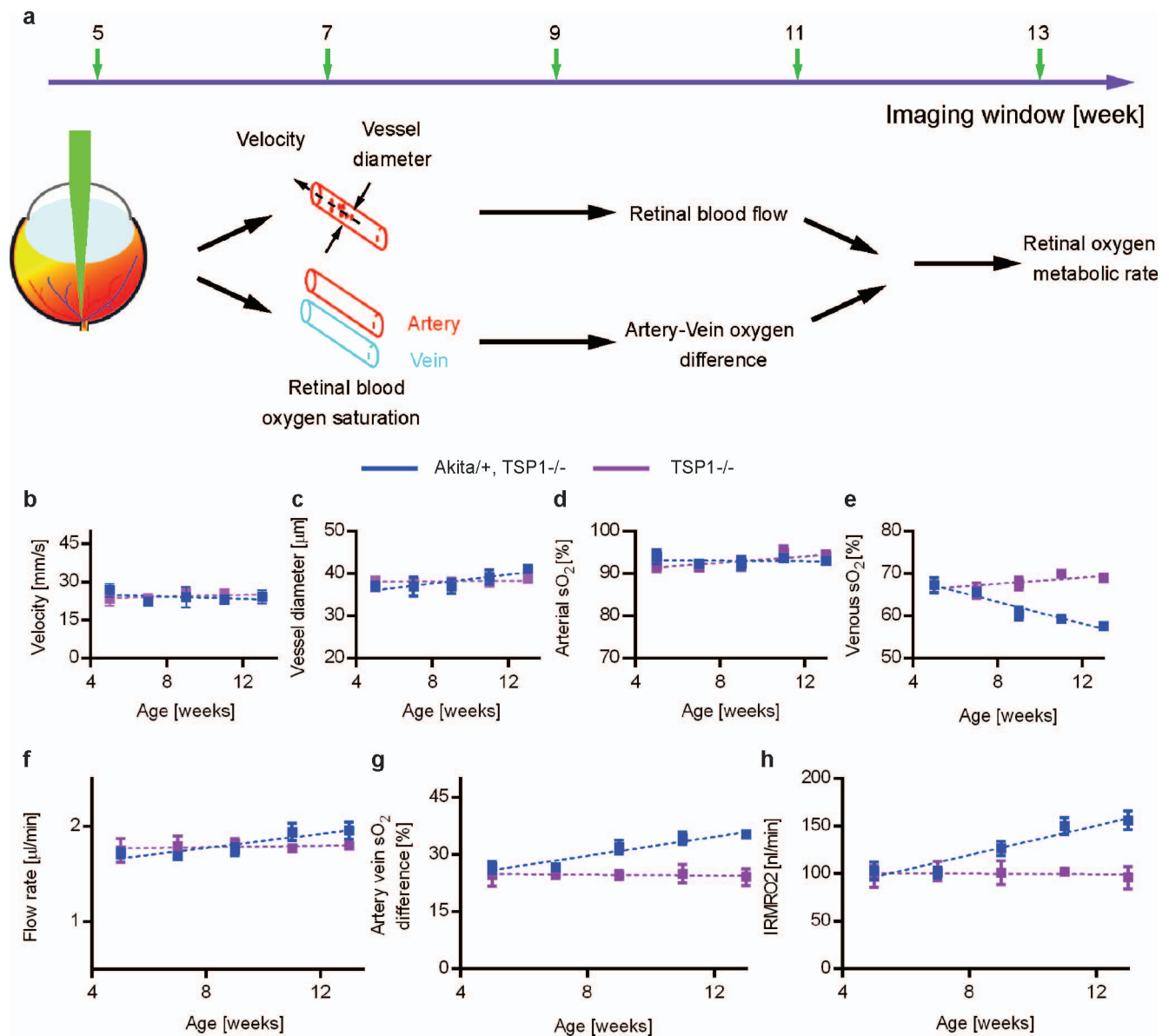
FIGURE 5. Longitudinal monitoring retinal flow, sO$_2$, and IRMRO$_2$ for both DR mice and control mice from 5 to 13 weeks of age. (a) Schematic of retinal oxygen metabolism measurement. (b) Longitudinal monitoring results of mean retinal arterial blood velocity. (c) Longitudinal monitoring results of mean retinal arterial vessel diameter. (d) Longitudinal monitoring results of mean retinal arterial sO$_2$. (e) Longitudinal monitoring results of mean retinal venous sO$_2$. (f) Longitudinal monitoring results of mean retinal blood flow. (g) Longitudinal monitoring results of artery-vein sO$_2$ difference. (h) Longitudinal monitoring results of IRMRO$_2$.

IRMRO$_2$ (less than 5% in relative percentage change) (Figs. 5e, 5g, 5h).

DISCUSSION

In this study, we found increased IRMRO$_2$ at early diabetes when there were no detectable anatomical retinal vascular complications. There are possible mechanisms for the increased IRMRO$_2$ at early diabetes. First, retinal and choroidal circulations together provide retinal tissue oxygen and nutrients, with choroidal circulation nourishing the outer retina and retinal circulation supporting inner retina. Reduced choroidal blood flow rate[11] was reported in early-stage diabetic mice (1-month-old Akita/+, TSP1$^{-/-}$ mice), when no retinal structural changes were observable. Decreased choroidal flow can lower the choroidal oxygen supply for photoreceptors; however, to maintain the normal function of photoreceptors, enough oxygen is necessary. To compensate for decreased supply from the choroid in early-stage diabetes, photoreceptors have to extract more oxygen from the retinal circulation. In this view, the increased IRMRO$_2$ would reflect increased extraction to supply the outer retina, rather than an increase in the utilization of oxygen in the inner retina. Second, high blood glucose in early diabetes prompts mitochondria to generate more reactive oxygen species (ROS).[27] In the presence of high ROS, mitochondrial uncoupling is activated to reduce ROS production[28]; however, increased mitochondrial uncoupling will contribute to increased oxygen consumption.[29]

Our results also imply that the increased IRMRO$_2$ at early diabetes is mainly from the decreased retinal venous sO$_2$ levels associated with the increased retinal artery-vein sO$_2$ differences, instead of the variation of retinal blood flow rate. This may

be reasonable for early diabetes in which no retinal microvasculature complications were observable. In early diabetes, the unchanged blood flow can be explained by the Hagen-Poiseuille law. According to the Hagen-Poiseuille law, blood flow rate is determined by the pressure drop across the vessel and the vessel diameter.[30] For one thing, the pressure drop across inner retinal vasculature depends on the systemic arterial and venous pressures as well as the intermediate resistance of the capillary network. The systemic arterial and venous pressures are likely the same between early-stage diabetic mice and control mice.[31] Histologic examination in our experiments found no microvascular changes in diabetic mice, which may indicate normal retinal intermediate resistance. In such a scenario, the pressure drop across the inner retina should be normal for diabetic mice. For another, we found unchanged retinal vessel diameters in diabetic mice. Thus, the retinal blood flow rate was expected to be normal in early diabetes, as we observed in the longitudinal monitoring experiments. With unchanged blood flow rate, the elevated inner retinal oxygen metabolism in diabetic mice is due to the decrease in venous sO_2 and increase in the artery-vein sO_2 difference.

Previous studies have reported retinal tissue hypoxia in DR,[32,33] which, however, are different from the increased $IRMRO_2$ we observed. As we considered, several factors can explain such discrepancies. First, the imaging time points were different. DR is a dynamic disease, in which retinal oxygen metabolism may change with DR development. In this study, we focused on early diabetes when there are no observable microvascular complications. In comparison, the reported studies targeted DR, when retinal capillary dysfunctions are already present[34]; nonperfused retinal capillaries in DR can cause hypoxia. For another, reported studies applied multiwavelength fundus photography or hyperspectral photography to measure retinal sO_2 in DR.[10,35–37] Because of lack of depth resolution, performance of both fundus photography and hyperspectral photography are sensitive to light scattering in retinal tissue and variation of local retinal geometrical parameters, including retinal vessel diameter, which usually generate biased sO_2 results.[13] In comparison, as a depth-resolved imaging technique, vis-OCT can precisely extract light absorption spectra from retinal blood vessels and accurately quantify sO_2.

Our study had a few limitations. First, there is a possibility that the volume of the retina in diabetic mice could have increased, resulting in the measured increase of $IRMRO_2$. Quantifying the whole retinal volume was not feasible with our current techniques and is a limitation to all present in vivo oxygen consumption studies. Moreover, several groups have studied the retinal thickness of Akita/+ mice, as a surrogate to the cell count, and found no significant changes in the thickness.[17,38] Second, because we focused on measuring the functional state of the retina with vis-OCT, we did not acquire OCT angiograms as part of our imaging protocol. Optical coherence tomography angiography has been recently reported using vis-OCT to study the capillary network in rodents.[21] Structural changes in the vasculature would be useful information to obtain, in addition to the measured functional parameters that we collected. For example, vessel tortuosity is associated with early-stage DR in humans.[9] However, it has been shown that the Akita/+ mouse does not develop retinal vascular changes until at least 6 months.[17] Future studies with vis-OCT will likely correlate longitudinal changes in vascular structure with functional oxygenation parameters. Last, a concern with vis-OCT is that the illumination beam, being visible, might activate retinal neurons and, through neurovascular coupling, alter the measured sO_2 or blood flow rate. Studies of retinal flicker in rodents suggest that this is unlikely, because the peak response for blood flow due to whole-eye retinal flicker in rodents is at 10 Hz.[39,40] In vis-OCT, A-lines are collected at 25 kHz, which is several orders of magnitude higher than in flicker studies. Moreover, the vis-OCT beam is focused by the lens of the rodent eye to a small spot on the retina, which is much smaller than the whole-eye illumination used in flicker experiments. Despite these facts, further studies are required to further investigate this issue.

In conclusion, we have applied vis-OCT to measure $IRMRO_2$ in Akita/+, $TSP1^{-/-}$ mice and controls. This is the first attempt to measure $IRMRO_2$ in a diabetic mouse model using OCT. We found that $IRMRO_2$ in diabetic mice was elevated from weeks 5 to 13 as compared with the controls. The elevation was primarily due to a measured decrease in venous sO_2, because arterial sO_2 and total blood flow rate remained insignificantly changed. During this same study period, we also found that PC and EC densities were the same between diabetic mice and control mice, which shows that the changes in $IRMRO_2$ occurred before vascular alterations. Using vis-OCT, future studies in human DR may potentially reveal similar changes in retinal metabolic variations observed in mouse models.

APPENDIX

Calculating sO_2 by LS Fitting

By substituting Equation 2 in Equation 1 and taking the natural log, Equation 1 can be rewritten as follows:

$$
\ln\left(\frac{I(\lambda)}{I_0(\lambda)}\right)
$$
$$
= \frac{1}{2}\ln(AR_0) - \frac{1}{2}\tau\ln(\lambda) - nd\left(\mu_{aHbO2}(\lambda) + 0.2\mu_{sHbO2}(\lambda)\right)sO_2
$$
$$
- nd\left(\mu_{aHb}(\lambda) + 0.2\mu_{sHb}(\lambda)(1 - sO_2)\right) \qquad (A1)
$$

Using this modified Equation A1, an LS fit can be performed to fit the OCT signal spectrum from a vessel, resulting in values for $ln(AR_0)$, sO_2, and τ.

Calculating the Doppler Angle

The Doppler angle θ can be calculated by inverting the cosine in the equation:

$$
\cos(\theta) = \frac{\overrightarrow{ES} \times \overrightarrow{NS}}{|\overrightarrow{ES}| \times |\overrightarrow{NS}|}, \qquad (A2)
$$

which results from the geometry shown in Figure 3a. The $\times$ denotes the vector dot product; $\overrightarrow{ES}$ and $\overrightarrow{NS}$ are the direction of blood flow and the probing light, respectively. The $\overrightarrow{ES}$ and $\overrightarrow{NS}$ were determined by the coordinates of E, S, and N. The E and S

represent the center points of the sample vessel within the small and big circular B-scan images; N signifies the nodal point of the eye. Coordinates of E, S, and N were derived from vessel centers within the circular B-scan images, as shown in Figure 3b. For simplicity, we assumed the coordinates of a sample vessel center positions (Fig. 3a) were (φ_1, D_1) and (φ_2, D_2) within the inner and outer circular B-scans; we also assumed the mouse eyeball diameter was b (the reported value is approximately 3 mm),[41] which was the length of NO. The diameters of the big ring and the small ring on the retina were r_1 and r_2. The coordinates of E, S, and N were estimated as follows[12]:

$$
\begin{aligned}
E &= \left(r_1 \times \cos(\varphi), r_1 \times \sin(\varphi_1), \left(D_1 + (r_1^2 + b^2)^{1/2} - b \right) \right. \\
&\quad \left. \cdot \cos(\phi_1) \right) \\
&= \left(b \times \tan(\phi_1) \times \cos(\varphi_1), b \times \tan(\phi_1) \times \sin(\varphi), \right. \\
&\quad \left. \left(D_1 + \left(\left(b \times \tan(\phi_1) \right)^2 + b^2 \right)^{1/2} - b \right) \cdot \cos(\phi) \right)
\end{aligned} \quad (A3)
$$

$$
\begin{aligned}
S &= \left(r_2 \times \cos(\varphi_2), \left(D_2 + (r_2^2 + b^2)^{1/2} - b \right) \cdot \cos(\phi_2) \right) \\
&= \left(b \times \tan(\varphi_2) \times \cos(\varphi_2), b \times \tan(\phi_2) \times \sin(\varphi_2), \right. \\
&\quad \left. \left(D_2 + \left(\left(b \times \tan(\phi_2) \right)^2 + b^2 \right)^{1/2} - b \right) \cdot \cos(\phi_2) \right)
\end{aligned} \quad (A4)
$$

$$
N = (0, 0, b) \quad (A5)
$$

With these equations, the Doppler angles were calculated.

References

1. Antonetti DA, Klein R, Gardner TW. Diabetic retinopathy. *N Engl J Med*. 2012;366:1227–1239.
2. Yau JW, Rogers SL, Kawasaki R, et al. Global prevalence and major risk factors of diabetic retinopathy. *Diabetes Care*. 2012;35:556–564.
3. Simo R, Hernandez C. Novel approaches for treating diabetic retinopathy based on recent pathogenic evidence. *Prog Retin Eye Res*. 2015;48:160–180.
4. Patel A, MacMahon S, Chalmers J, et al. Intensive blood glucose control and vascular outcomes in patients with type 2 diabetes. *N Engl J Med*. 2008;358:2560–2572.
5. Alder VA, Su EN, Yu DY, Cringle SJ, Yu PK. Diabetic retinopathy: early functional changes. *Clin Exp Pharmacol Physiol*. 1997;24:785–788.
6. Kowluru RA, Chan PS. Oxidative stress and diabetic retinopathy. *Exp Diabetes Res*. 2007;2007:43603.
7. Boulton M, Cai J. The pathogenesis of diabetic retinopathy: old concepts and new questions. *Eye*. 2002;16:242260.
8. Stitt AW, Gardiner TA, Archer DB. Histological and ultrastructural investigation of retinal microaneurysm development in diabetic patients. *Br J Ophthalmol*. 1995;79:362–367.
9. Sasongko MB, Wong TY, Nguyen TT, Cheung CY, Shaw JE, Wang JJ. Retinal vascular tortuosity in persons with diabetes and diabetic retinopathy. *Diabetologia*. 2011;54:2409–2416.
10. Tayyari F, Khuu LA, Flanagan JG, Singer S, Brent MH, Hudson C. Retinal blood flow and retinal blood oxygen saturation in mild to moderate diabetic retinopathy. *Invest Ophthalmol Vis Sci*. 2015;56:6796–6800.
11. Muir ER, Renteria RC, Duong TQ. Reduced ocular blood flow as an early indicator of diabetic retinopathy in a mouse model of diabetes. *Invest Ophthalmol Vis Sci*. 2012;53:6488–6494.
12. Song W, Wei Q, Liu W, et al. A combined method to quantify the retinal metabolic rate of oxygen using photoacoustic ophthalmoscopy and optical coherence tomography. *Sci Rep*. 2014;4:6525.
13. Liu W, Jiao S, Zhang HF. Accuracy of retinal oximetry: a Monte Carlo investigation. *J Biomed Opt*. 2013;18:066003.
14. Jo DH, Cho CS, Kim JH, Jun HO, Kim JH. Animal models of diabetic retinopathy: doors to investigate pathogenesis and potential therapeutics. *J Biomed Sci*. 2013;20:38.
15. Robinson R, Barathi VA, Chaurasia SS, Wong TY, Kern TS. Update on animal models of diabetic retinopathy: from molecular approaches to mice and higher mammals. *Dis Model Mech*. 2012;5:444–456.
16. Sorenson CM, Wang S, Gendron R, Paradis H, Sheibani N. Thrombospondin-1 deficiency exacerbates the pathogenesis of diabetic retinopathy. *J Diabetes Metab*. 2013;(suppl 12):s12-005.
17. Han Z, Guo J, Conley SM, Naash MI. Retinal angiogenesis in the Ins2Akita mouse model of diabetic retinopathy. *Invest Ophthalmol Vis Sci*. 2013;54:574–584.
18. Yi J, Wei Q, Liu W, Backman V, Zhang HF. Visible-light optical coherence tomography for retinal oximetry. *Opt Lett*. 2013;38:1796–1798.
19. Yi J, Liu W, Chen S, et al. Visible light optical coherence tomography measures retinal oxygen metabolic response to systemic oxygenation. *Light Sci Appl*. 2015;4:e334.
20. Liu W, Yi J, Chen S, Jiao S, Zhang HF. Measuring retinal blood flow in rats using Doppler optical coherence tomography without knowing eyeball axial length. *Med Phys*. 2015;42:5356–5362.
21. Chen S, Yi J, Zhang HF. Measuring oxygen saturation in retinal and choroidal circulations in rats using visible light optical coherence tomography angiography. *Biomed Opt Express*. 2015;6:2840–2853.
22. Dai C, Liu X, Zhang HF, Puliafito CA, Jiao S. Absolute retinal blood flow measurement with a dual-beam Doppler optical coherence tomography. *Invest Ophthalmol Vis Sci*. 2013;54:7998–8003.
23. Wang Y, Bower BA, Izatt JA, Tan O, Huang D. Retinal blood flow measurement by circumpapillary Fourier domain Doppler optical coherence tomography. *J Biomed Opt*. 2008;13:064003.
24. Singh AS, Kolbitsch C, Schmoll T, Leitgeb RA. Stable absolute flow estimation with Doppler OCT based on virtual circumpapillary scans. *Biomed Opt Express*. 2010;1:1047–1058.
25. Song W, Wei Q, Feng L, et al. Multimodal photoacoustic ophthalmoscopy in mouse. *J Biophotonics*. 2013;6:505–512.
26. Yi J, Chen S, Shu X, Fawzi AA, Zhang HF. Human retinal imaging using visible-light optical coherence tomography guided by scanning laser ophthalmoscopy. *Biomed Opt Express*. 2015;6:3701.
27. Inoguchi T, Li P, Umeda F, et al. High glucose level and free fatty acid stimulate reactive oxygen species production through protein kinase C—dependent activation of NAD(P)H oxidase in cultured vascular cells. *Diabetes*. 2000;49:1939–1945.
28. Echtay KS, Roussel D, St-Pierre J, et al. Superoxide activates mitochondrial uncoupling proteins. *Nature*. 2002;415:96–99.
29. Friederich M, Fasching A, Hansell P, Nordquist L, Palm F. Diabetes-induced up-regulation of uncoupling protein-2 results in increased mitochondrial uncoupling in kidney proximal tubular cells. *Biochim Biophys Acta*. 2008;1777:935–940.
30. Ganesan P, He S, Xu H. Analysis of retinal circulation using an image-based network model of retinal vasculature. *Microvasc Res*. 2010;80:99–109.
31. Soetikno BT, Yi J, Shah R, et al. Inner retinal oxygen metabolism in the 50/10 oxygen-induced retinopathy model. *Sci Rep*. 2015;5:16752.

32. Linsenmeier RA, Braun RD, McRipley MA, et al. Retinal hypoxia in long-term diabetic cats. *Invest Ophthalmol Vis Sci*. 1998;39:1647–1657.

33. de Gooyer TE, Stevenson KA, Humphries P, Simpson DA, Gardiner TA, Stitt AW. Retinopathy is reduced during experimental diabetes in a mouse model of outer retinal degeneration. *Invest Ophthalmol Vis Sci*. 2006;47:5561–5568.

34. Frank RN. Diabetic retinopathy. *N Engl J Med*. 2004;350:48–58.

35. Khoobehi B, Firn K, Thompson H, Reinoso M, Beach J. Retinal arterial and venous oxygen saturation is altered in diabetic patients. *Invest Ophthalmol Vis Sci*. 2013;54:7103–7106.

36. Hardarson SH, Stefansson E. Retinal oxygen saturation is altered in diabetic retinopathy. *Br J Ophthalmol*. 2012;96:560–563.

37. Hammer M, Heller T, Jentsch S, et al. Retinal vessel oxygen saturation under flicker light stimulation in patients with nonproliferative diabetic retinopathy. *Invest Ophthalmol Vis Sci*. 2012;53:4063–4068.

38. Mclenachan S, Chen X, Mcmenamin PG, Rakoczy EP. Absence of clinical correlates of diabetic retinopathy in the Ins2Akita retina. *Clin Exp Ophthalmol*. 2013;41:582–592.

39. Shakoor A, Blair NP, Mori M, Shahidi M. Chorioretinal vascular oxygen tension changes in response to light flicker. *Invest Ophthalmol Vis Sci*. 2006;47:4962–4965.

40. Radhakrishnan H, Srinivasan VJ. Multiparametric optical coherence tomography imaging of the inner retinal hemodynamic response to visual stimulation. *J Biomed Opt*. 2013;18:086010.

41. Schmucker C, Schaeffel F. A paraxial schematic eye model for the growing C57BL/6 mouse. *Vision Res*. 2004;44:1857–1867.